Journal of Physics: Photonics

OPEN ACCESS

RECEIVED
21 April 2021

REVISED
29 July 2021

ACCEPTED FOR PUBLICATION
6 August 2021

PUBLISHED
24 August 2021

PAPER

Design and two-photon direct laser writing of low-loss waveguides, tapers and S-bends

Tigran Baghdasaryan*, Koen Vanmol, Hugo Thienpont, Francis Berghmans, Thomas Geernaert and Jürgen Van Erps

Vrije Universiteit Brussel, Department of Applied Physics and Photonics, Brussels Photonics (B-PHOT) and Flanders Make, Pleinlaan 2, 1050 Brussels, Belgium

* Author to whom any correspondence should be addressed.

E-mail: tigran.baghdasaryan@vub.be

Keywords: direct laser writing, two-photon polymerization, polymer waveguides, adiabatic tapers, S-bends, 3D waveguide components, fiber coupling

Abstract

Despite the rapid developments in the field of two-photon polymerization-based direct laser writing, limited attention has been paid to the efficient design of optical waveguide-based building blocks. To fill that gap, we have numerically investigated air-clad waveguides, tapers, and S-bends, with the aim to minimize insertion losses, whilst reducing the device sizes. We have first demonstrated waveguides with square and circular cross-sections that are mode-matched with single-mode optical fibers featuring insertion losses below −0.6 dB and −1.5 dB around 1550 nm for lengths of respectively 0.2 mm and 1 mm. We have also identified parabolic tapers that allow for adiabatic transition between a wide range of input and output waveguide sizes. These shapes allow, for example, tapering down from 15 μm to 2 μm diameter waveguides over a length as short as 43.2 μm. We have fabricated a series of such components and confirmed their nearly lossless performance with insertion loss measurements. Finally, we have designed and optimized S-bends with Bezier curve shapes. As a proof-of-principle demonstration, we have fabricated a 160 μm long S-bend that offsets the waveguide axis by 50 μm. The insertion loss of the resulting 400 μm long component, which also included two parabolic tapers, was less than −1.7 dB. Apart from providing design rules and ready-to-use recipes for fabricating low-loss 3D-printed waveguide-based building blocks, we project that our work will spark the development of a series of efficient photonic devices that rely on these components and that can be exploited in diverse application fields.

1. Introduction

Direct laser writing using two-photon polymerization (2PP) is an emerging technology that enables high-speed single-step fabrication at the micron scale, whilst offering full 3D printing capabilities [1, 2]. This technology is exploited for fabricating micro- and nano-photonic devices in optically transparent polymers, with high-resolution and sub-micrometer accuracy and this for a wide variety of applications including imaging [3], optical communications [4–7] and sensing [8, 9].

Low-loss interfacing between optical fibers and photonic integrated circuits is an example of a challenge that can be addressed using direct laser writing. For example, Lindenmann *et al* and Billah *et al* used 2PP-written waveguides and tapers to couple multicore fibers to planar silicon chips [5, 6]. More recently, Gehring *et al* used direct laser written waveguides, bends and tapers for broadband light coupling from photonic integrated circuits to fibers [10]. We have already contributed to these efforts as well, by demonstrating waveguide tapers on optical fiber tips for fiber-to-fiber and fiber-to-chip connections [11–13]. The issue of fiber-to-polymer waveguide coupling itself has also been recently addressed by Kumar *et al*, who used a silicon nitride grating coupler with a taper to interface with a 2 × 2 μm^2 3D-printed polymer waveguide featuring coupling efficiencies of −3.55 dB in the C-band and −2.92 dB in the L-band, for a single polarization [14]. Besides coupling structures, photonic sensor structures can also be developed based on

2PP-writing. Wei *et al* fabricated a Mach–Zehnder interferometer, micro-ring resonator and phase-shifted gratings with a 2PP approach for refractive index sensing and ultrasound detection [8, 15, 16]. Kelemen *et al* developed a direct laser written ring resonator-based biosensor [9]. Zhang *et al* used the tip of a multi-core fiber to fabricate micropillar waveguides, prisms, tapers and ring resonators for vapor sensing [17].

Although many waveguide components such as tapers, bends, splitters, ring resonators, gratings and devices based on those have been demonstrated with 2PP-based 3D-printing technology, in-depth studies combining numerical simulations with dedicated fabrication methods that are supplemented with thorough characterizations of the individual components are often missing. The proposed solutions are often sub-optimal and the choices for the geometries and sizes remain mostly unjustified. For example, some of the results rely on non-mode-matched waveguides for interfacing with an optical fiber [7–9, 15, 18, 19], which in their turn lead to significant insertion loss. Additionally, when tapers are used as mode converters they are often linearly tapered and as such are often not the best choice in terms of length and losses [5, 6, 8–10, 14, 15, 17, 18]. Finally, some authors prefer to use circular waveguides, whilst others use square or rectangular-shaped waveguides without justifying their choice. Whilst we understand that this may be driven by the limits of the available fabrication tools and materials, and by the desire to avoid too complex manufacturing processes, there is ample room for improvements. Our objective is therefore to pave the way towards improved direct laser written 2PP photonic waveguide-based components.

Defining design rules and optimizing these important building blocks to minimize optical losses is indeed critical for the further development of the field [7, 14, 19]. To do so, we first developed a dedicated numerical and experimental methodology that can be used to study and optimize various 3D-printed photonic waveguide components and devices. Then we used that methodology to study 3D-printed waveguides, parabolic shaped tapers and S-shaped waveguide bends. Our design cycle includes modeling, fabrication and characterization, and aims to minimize optical losses, whilst enabling fast and repeatable fabrication and characterization.

Our paper is structured as follows: in the second section, we introduce our modeling and fabrication approach, as well as our methodology for characterizing the waveguide components. In section 3.1, we deal with our modeling results for square and circular cross-section waveguides, parabolic tapers, and S-shaped waveguide bends. Section 3.2 reports on proof-of-concept demonstrations of those waveguide components fabricated with direct laser writing as well as on the results of insertion loss measurements. We discuss our findings in section 4 and we close and conclude the paper with section 5.

2. Methods and materials

For our numerical studies, we have exploited the commercially available Ansys/Lumerical Inc. DEVICE Suite software, in which we mainly used the MODE waveguide and finite difference time domain (FDTD) 3D electromagnetic simulators [20]. For the actual direct laser writing-based fabrication, we have used the Nanoscribe Photonic Professional GT+ direct laser writing workstation that enables 2PP to fabricate 3D structures in specific polymers [21]. All the devices described later in this paper were manufactured with a line-by-line scanning approach using galvanometric mirrors and plane-by-plane stacking using a piezo stage. This was done using a 63× objective lens in the dip-in lithography mode in Nanoscribe's proprietary IP-Dip® photoresist. Note that the refractive index of polymerized IP-Dip® is around 1.53 at 1550 nm [22]. Images of the fabricated structures were taken using a Hirox SNE4500M table-top scanning electron microscope (SEM).

This brings us to a specific aspect of our work: to enable repeatable and fast characterization of the different 3D-printed waveguide components, we have developed a dedicated methodology for printing whilst allowing for easy coupling of optical fibers to the components under test. Direct laser writing is routinely implemented on a planar substrate. To allow for free-space coupling of the printed components with optical fibers for insertion loss measurements, we have raised the waveguide component so as to reach the height of the fiber core by means of dedicated 3D-printed support structures. This approach is illustrated in figure 1, which uses an example of a straight waveguide with a square cross-section. Two fibers can be placed straightforwardly at each end of the component under test for in- and out-coupling of optical power. The waveguide's center is positioned at a height of 62.5 μm to align with the center of the core of a 125 μm diameter single-mode fiber (SMF), while the waveguide itself rests on a mechanical support by ways of a narrow separation ridge. The support is designed to have a sufficiently large contact area in view of ensuring adhesion to the substrate carrier during 2PP-based writing. Triangular arches were added to avoid delamination caused by the volume shrinkage of the polymerized photoresist during the development stage. The ridge between waveguide and support should be sufficiently narrow not to affect the guiding properties of the waveguide. Finally, and to facilitate accurate fiber alignment with the 3D-printed component, we also pre-fabricated V-grooves at both sides, which are clearly visible in the front view provided in figure 1.

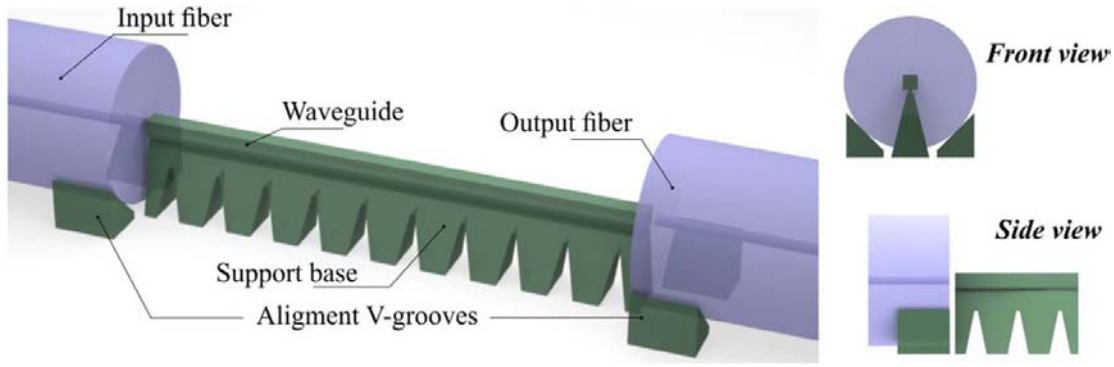

Figure 1. Concept of the fiber-component-fiber configuration illustrated with a waveguide that features a square cross-section.

We have performed insertion loss measurements on all the fabricated devices using a C- and L-band amplified spontaneous emission (ASE) source from NP Photonics in combination with a Newport 2832-c power meter equipped with an 818-IR detector. To start, we used an optical fiber patch cord made from standard G.652 telecom SMF and equipped with FC connectors at both ends to connect the detector to the source. We took the reference optical power measurement M1 once the equipment was warmed up and the power reading had stabilized. Then we cleaved the patch cord in the middle and mounted the cleaved fiber ends on three-axes manual translation stages. This was done without unmating and remating the FC connectors at both the source and power meter side to avoid introducing measurement uncertainties due to variations in coupling losses at the connectors. By using a microscope, we positioned the cleaved fiber ends in the pre-fabricated V-grooves on each side of the 3D-printed component under test, we finely tuned the positions of the fibers in the V-grooves without making physical contact with the polymer waveguide to maximize the coupling and we took the second power reading M2. We then calculated the insertion loss of the device as M1–M2 (expressed in dB). To verify the repeatability of the fabrication, we have fabricated several identical components and we did measure the insertion loss for each of them following the procedure explained above. This allowed calculating the insertion loss averaged over several identical components and the standard deviations provided in section 3.2. For certain components, we have also measured the spectral transmission using an ANDO Optical Spectrum Analyzer in combination with the same C- and L-band ASE source.

3. Results

We start with our modeling results. We have modeled air-clad waveguides with both square and circular cross-sections and with these we studied straight waveguides, parabolic tapers and S-bends that allow interfacing between two SMFs. All our analyses are carried out in the wavelength range from 1500 to 1600 nm and consider two orthogonal polarization states transverse electric (TE) and transverse magnetic (TM). After the discussion on the modeling results, we report on the fabrication results as well as on the characterization by means of insertion loss measurements, whilst comparing the measurement with the modeling data.

3.1. Modeling

3.1.1. Fiber coupling waveguides

The premise of our study was the intention to provide for low-loss interfacing between two SMFs using dedicated waveguide structures. We targeted waveguide dimensions allowing for maximal overlap between the fundamental mode of the 3D-printed waveguide and that of an SMF-28® optical fiber and to do so we used the MODE waveguide simulator. The simulation results are shown in figure 2 for waveguides with square and circular cross-sections: we calculated the power overlap of the modes at 1550 nm whilst varying the cross-sectional dimension of the waveguide. For the waveguides with smaller size, the mode size is smaller than that of the SMF-28® fiber, which results in higher mode overlap loss. On the other hand and for the larger waveguide sizes, the mode size exceeds that of the SMF-28® fiber, which in its turn also causes higher mode overlap loss. For IP-Dip® waveguides, we achieve best mode matching (and thus best coupling) with an SMF-28® fiber for a 14×14 μm^2 square waveguide and a 15 μm diameter circular waveguide. In both cases, the simulations predict a similar minimal coupling loss of -0.19 dB.

Note that a free-space coupling scheme also leads to additional loss due to Fresnel reflections and the potential Fabry–Pérot etalon formed by the air gap between the fiber and waveguide facets [23]. To account

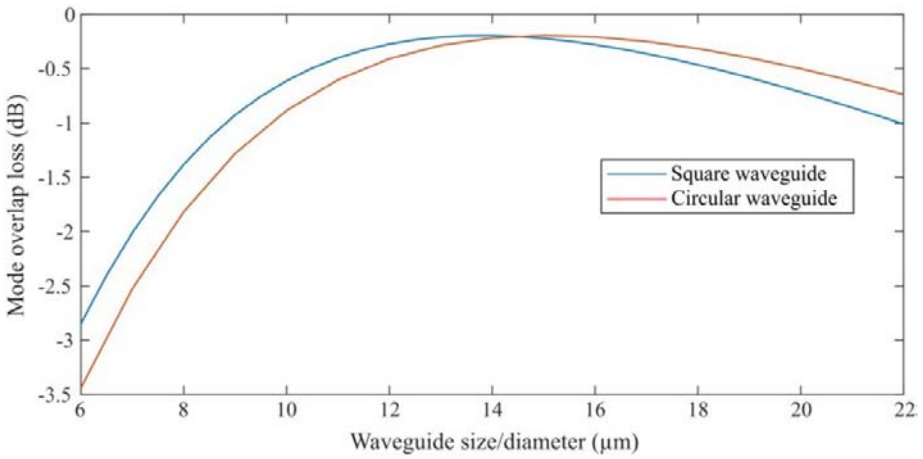

Figure 2. Mode overlap loss (in dB) as a function of waveguide cross-sectional dimension, when coupling an SMF-28® fiber to a 3D-printed waveguide, for square and circular waveguide cross-sections.

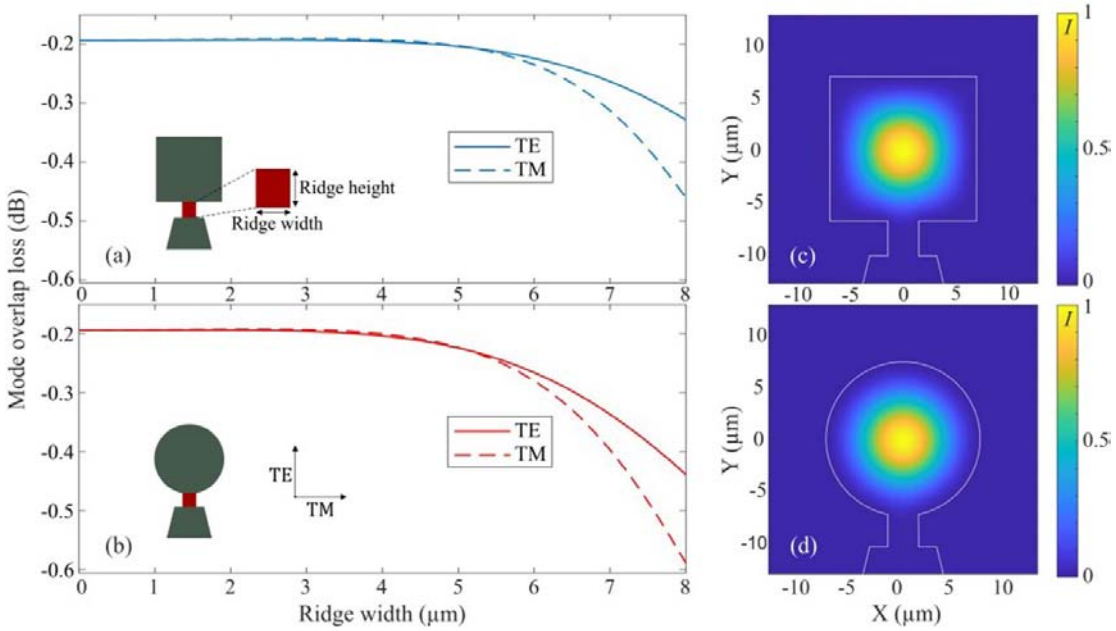

Figure 3. Mode overlap loss (in dB) as a function of the width of the ridge between waveguide and support, when coupling to SMF-28® fiber for waveguides with (a) square and (b) circular cross-sections. The mode intensity distributions are shown for a ridge with a width of 3 μm. The color scale is normalized.

for these effects, we carried out full 3D FDTD simulations with the Ansys/Lumerical Inc. FDTD 3D electromagnetic simulator in view of calculating the free-space coupling efficiency. The simulations reveal that the coupling loss averaged over the fiber-to-waveguide gap (with a width ranging from 1 to 5 μm) equals −0.5 dB, with a minimum value of −0.19 dB and a maximum value of −0.82 dB. The results are very much identical whether one considers monochromatic light at 1550 nm or a broadband light source spanning the range from 1500 to 1600 nm. In both cases, Fabry–Pérot oscillations are present with similar minimum and maximum values, depending on the gap width.

The waveguide rests on the mechanical support by means of a narrow ridge (see figure 1 and insets in figure 3(a)). The presence of this ridge should not affect the optical waveguiding properties. We have therefore investigated the influence of said ridge on the guiding properties of the waveguides and on the coupling to SMF-28® fiber. To do so, we considered the best waveguides in terms of losses, i.e. those with dimensions of 14 × 14 μm^2 (square) and 15 μm diameter (circular), and their fundamental modes at two orthogonal polarizations (TE and TM). We fixed the height of the ridge to 3 μm, we varied the width of the ridge and we monitored the power overlap between the fundamental mode of the waveguide and the SMF-28® fiber. Figures 3(a) and (b) show the modeling results for varying ridge widths, from 0 to 8 μm. A

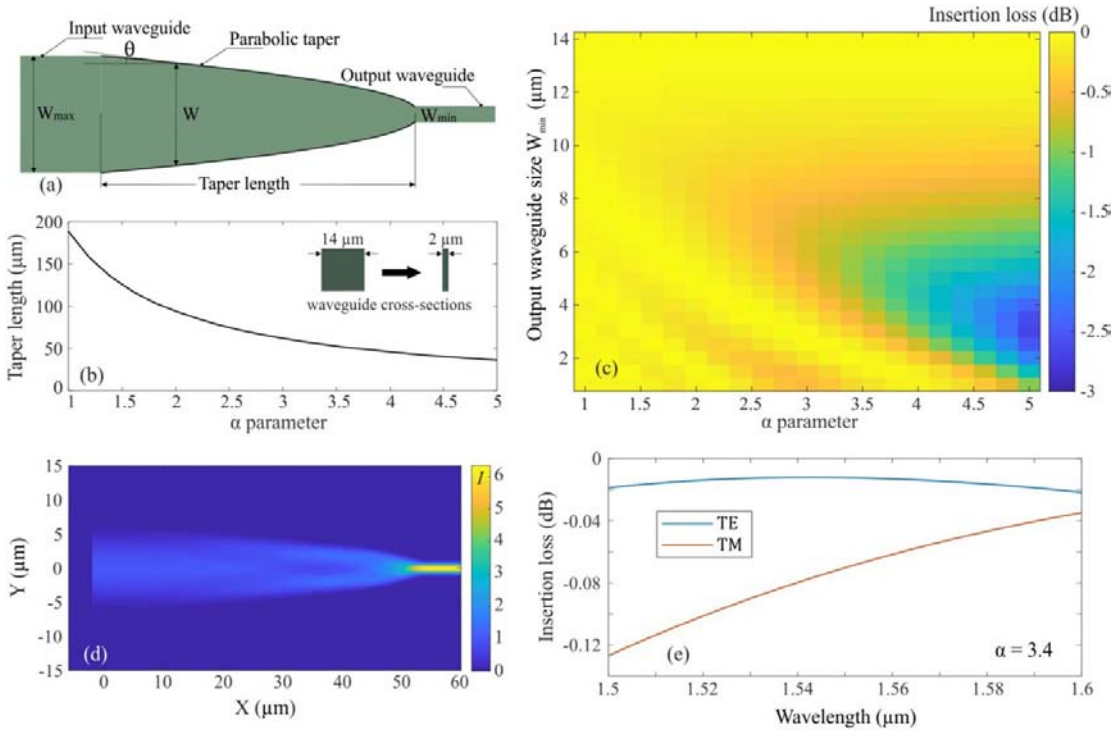

Figure 4. (a) Top view of an adiabatic taper and definitions of its main geometrical parameters. (b) Dependence of the taper length on the parameter α shown for the example of input and output waveguides with respectively 14×14 μm^2 and 14×2 μm^2 cross-sections. (c) Dependence of the transmission on the α parameter and the output waveguide size 14 μm $\times$ W_{min}, for TE-polarized modes at 1550 nm. (d) Intensity distribution in the taper from 14×14 μm^2 and 14×2 μm^2 cross-section waveguide with $\alpha = 3.4$ and with a color scale that is normalized to the intensity of the incident mode. (e) Dependence of the insertion loss on wavelength for the two orthogonally polarized fundamental TE- and TM-modes.

ridge width up to 4 μm has a negligible influence on the mode overlap loss between the fiber and the 3D-printed waveguides, for both the square and circular waveguide cross-sections. Above a ridge width of 4 μm, loss increases significantly and differences for TE- and TM-polarized modes become obvious, with TM-polarized modes featuring the highest loss values.

In addition, we have modeled the difference of the effective refractive indices or birefringence of the waveguides as a function of the ridge width. For a ridge width up to 4 μm, the birefringence is less than 1×10^{-5} for both types of waveguides and it rapidly increases for larger ridge sizes. The confinement loss for the considered waveguides remains negligible for ridge widths up to 4 μm. Based on those results, we have opted to work with a ridge width of 3 μm. Figures 3(c) and (d) show the normalized mode intensity distributions for both waveguides cross-sections with a 3×3 μm^2 ridge: this evidences that the ridge has limited to no influence on the mode confinement in the waveguide.

3.1.2. Waveguide tapers

A second building block for 3D-printed integrated photonic devices is a waveguide taper. This is conventionally used to adapt the mode size in view of coupling between waveguides with different cross sections, which is an often-required functionality.

We started our study with the waveguide cross-sections described in the previous sub-section. The goal was to identify taper shapes with shortest length that allow coupling light adiabatically from fiber-coupling waveguides to waveguides with smaller sizes. To design such a taper, we exploited the classical approach proposed by Milton and Burns [24]. They defined the criterion for adiabatic operation of the tapers as:

$$\theta < \lambda_g / 2W \tag{1}$$

where θ is the tangential angle of the taper at the location with width W, while λ_g is the wavelength of the fundamental mode of the waveguide at that same location. The latter can be expressed by means of the effective index of the mode n_{eff} as $\lambda_g = \lambda_0 / n_{eff}$, where λ_0 is the wavelength in vacuum. Figure 4(a) shows a top view of such an adiabatic taper and defines its main geometrical parameters.

To quantify to what extent we comply with the criterion, we introduced the parameter α, as also done in [24, 25]:

$$\theta = \alpha\lambda_g/2W. \tag{2}$$

For large α, the taper is shorter and hence beneficial from the practical standpoint, as it is more compact and allows for a shorter 3D-printing time. We therefore seek the upper limit of α that still allows for an adiabatic transition for 2PP-printed waveguides in IP-Dip®.

First, we considered a waveguide with a 14×14 μm^2 square cross-section and a one-dimensional planar taper down to a waveguide with a $14 \times W_{min}$ μm^2 rectangular cross-section, where W_{min} is the width of the output waveguide after tapering. Using the MODE waveguide simulator, we have calculated the effective indices for waveguide widths varying between $W_{max} = 14$ μm and $W_{min} = 1$ μm and we have used this data to construct the taper shape according to equation (2) for different values of α. The resulting shape of the taper is a perfect parabola and very often the term parabolic taper is used in literature when referring to such an adiabatic taper. Note that we have already introduced parabolic tapers for waveguides with circular cross-sections in [12] in view of fiber-to-chip coupling. Here, we conduct a more extended study and we look into different waveguide shapes and parameters. Figure 4(b) shows the results for the dependence of the taper length on α for a target waveguide cross-section of 14×2 μm^2. For $\alpha = 1$, the taper length is 188 μm, while for $\alpha = 5$ it is around 36 μm.

We modeled the transmission through such tapers as a function of the parameter α and a range of W_{min} values using the varFDTD solver functionality of the MODE simulator. The solver can be used for planar integrated optical systems and truncates 3D wave propagation problems into 2D problems using an approach identical to the effective index method [26]. Truncating the problem from 3D to 2D allows decreasing the simulation time whilst carrying out parameter sweep analyses. Figure 4(c) shows the results at 1550 nm and for TE-polarized fundamental modes, and for tapers with W_{min} ranging from 1 to 14 μm. Recall that $W_{min} = 14$ μm corresponds to the untapered case. Despite the geometrical asymmetry and the significant birefringence of the output waveguides, the results for TE- and TM-polarized modes were very similar. Hence and for the sake of conciseness, we only report the results for TE-polarized modes. These results indicate that there is a vast parameter region within which adiabatic transition is possible. For tapers down to $W_{min} = 8$ μm, the maximal value of α for an adiabatic transition decreases with decreasing waveguide size. However, beyond a valley with insertion loss reaching nearly -3 dB, we obtain a region of nearly lossless propagation for larger values of α (i.e. smaller taper lengths). For example, for $W_{min} = 6$ μm, a maximum transmission of 99% can be achieved for $\alpha = 1.6$, while for $W_{min} = 2$ μm, the same transmission is achieved for $\alpha = 3.4$. This seems counterintuitive: for $W_{min} = 6$ μm, the shortest taper length for an adiabatic transition is 118 μm, while for $W_{min} = 2$ μm the shortest length is only 55 μm. For TM-polarized fundamental modes, we find an identical behavior for slightly smaller values of α ($\alpha = 3.2$ for $W_{min} = 2$ μm). Note that in the regions with low transmission, the loss is due to coupling to higher order modes, since the transmission is calculated for the fundamental mode.

Figure 4(d) shows the intensity distribution normalized to the intensity of the incident mode in the taper with $\alpha = 3.4$, between waveguides with 14×14 μm^2 down to 14×2 μm^2 cross-sections. Figure 4(e) shows the wavelength dependence of the transmission from 1500 to 1600 nm. As this taper was optimized for the TE-polarized mode, there is low wavelength dependence with insertion loss values between -0.01 and -0.02 dB. For the same taper, the TM-polarized mode shows a slightly stronger wavelength dependence with an insertion loss around -0.13 dB at 1500 nm, and a minimum of -0.03 dB at 1600 nm. The slight difference in wavelength dependence for the TE and TM polarized modes can be explained by the birefringent nature of the tapered waveguide. For unpolarized broadband light in the range from 1500 to 1600 nm, the average insertion loss is below -0.05 dB. Anyhow, we can safely state that the spectral and polarizationdependence for the rectangular shaped optimal adiabatic tapers in the wavelength range from 1500 to 1600 nm is very low, which is a definite advantage for these components.

We have performed a similar study for tapers with a circular cross-section as well. We started from a waveguide with a 15 μm diameter (cf also above). We have also investigated the influence of the α parameter for different diameters of the output waveguide. For that purpose, we have carried out full 3D FDTD simulations, with results shown in figure 5(a). We have deliberately limited the study to output waveguide diameters ranging from 1 to 8 μm due to the extended simulation time. We observe a similar behavior as for the square tapers with a region of high transmission extending to larger α when decreasing the output waveguide diameter. However, the region is slightly shifted to higher α values, resulting in even shorter tapers. For an output waveguide diameter of 2 μm, adiabatic transmission is observed for $\alpha = 4.2$, which results in a taper length of 43.2 μm.

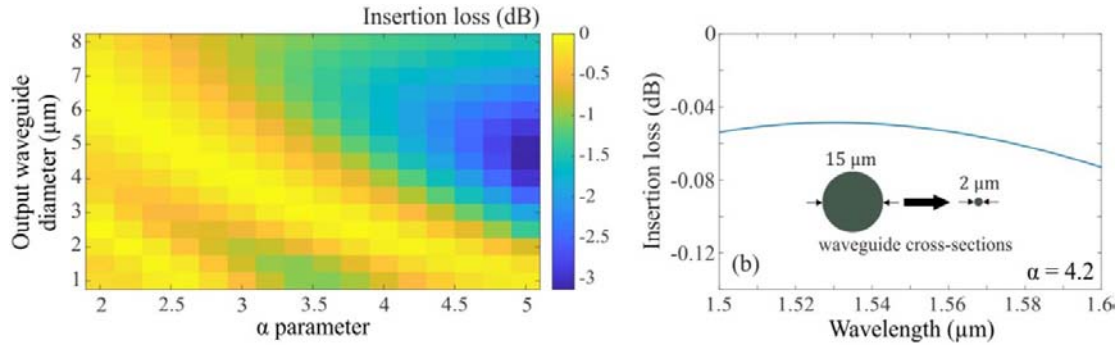

Figure 5. (a) Dependence of the transmission through a circular taper on the α parameter and the output waveguide diameter, for a TE-polarized mode at 1550 nm; and (b) dependence of the insertion loss on wavelength for a taper with $\alpha = 4.2$.

We also studied the spectral dependence of the transmission for the example of a 15 μm to 2 μm diameter taper with $\alpha = 4.2$. The results are shown in figure 5(b) (the inset shows the waveguide cross-sections). The results in the range between 1500–1600 nm show a very weak wavelength dependence with an average insertion loss of −0.06 dB.

3.1.3. Waveguide S-bends

Finally, we have also investigated 3D-printed S-shaped waveguide bends or S-bends that enable offsetting waveguide axes with respect to each other with minimal losses, whilst keeping most of the energy in the fundamental mode of the waveguide. An important aspect of the design is the shape of the curve that connects straight sections of the input and the output waveguides. Different approaches have already been described in open literature: from basic circular section curves to so-called Euler and Bezier curves [27]. Our approach is based on Bezier curves, which were initially developed for computer graphics to generate smooth curve transitions [28], with the intention to describe a gradual change of the radius of curvature. Such curves are defined by a set of control points, as illustrated in figure 6(a). From those, we consider the S-bend with features summarized in figure 6(b). The control points P0 and P3 define the start and end points, while P1 and P2 define the shape of the curve. For an S-bend, having P0 and P1 along the axis of the input waveguide and P2 and P3 along the axis of the output waveguide ensures that the Bezier curves are well interfaced with straight waveguide sections. We have considered the case where P1 and P2 are positioned in the middle of the S-bend length. Our initial simulations have shown that the position of these points influences the performance of the S-bend, but we leave the search for alternative configurations to future research and we limited ourselves here to this one case.

We initiated our study with a 14 × 14 μm^2 square cross-section waveguide, and the example presented here targets offsetting the waveguide axis by 50 μm. We started from 10 μm long straight input and output waveguide sections and we launched broadband light in the range from 1500 to 1600 nm into the input waveguide port. We monitored the insertion loss averaged over all wavelengths for the fundamental TE- and TM-modes. Figure 6(c) shows the results obtained with the varFDTD solver for the insertion loss through such a system, when the length of the S-bend is varied from 50 μm to 200 μm. The insertion loss exceeds −6.9 dB, which motivates the need for alternatives.

One approach for shortening the S-bend length and avoiding strong coupling from fundamental to higher order modes and hence allowing for low loss transmission is to decrease the waveguide cross-sectional size in the plane of the waveguide curvature. In the coordinate system defined in figure 6, this corresponds to the size along the Y-axis of the waveguide. Next, we modeled a waveguide with a 14 × 4 μm^2 cross-section. The 4 μm feature of the waveguide was chosen following feedback from fabrication trials and characterization cycles. This allowed demonstrating low loss transmission experimentally (cf section 4). Figure 6(d) shows the simulation results. Starting from a 150 μm long S-bend, the insertion loss stays below −0.4 dB with little polarization dependence, indicating that working with smaller size waveguides allows dramatically reducing the bend loss. In combination with our parabolic tapers, this allows designing low insertion loss S-bends in IP-Dip® with the 2PP printing technology. Figure 6(e) shows the intensity distribution in the bending plane for a 160 μm long S-bend, which clearly illustrates adiabatic transmission of the fundamental mode from the input waveguide to the output waveguide. Figure 6(e) reveals a periodic energy transfer from the fundamental mode to higher order modes, which can be observed from the regions with higher intensity in the bent section. This likely stems from higher order mode excitation and multimode interference induced by the bend. The length of the S-bend that we have chosen allows having only the

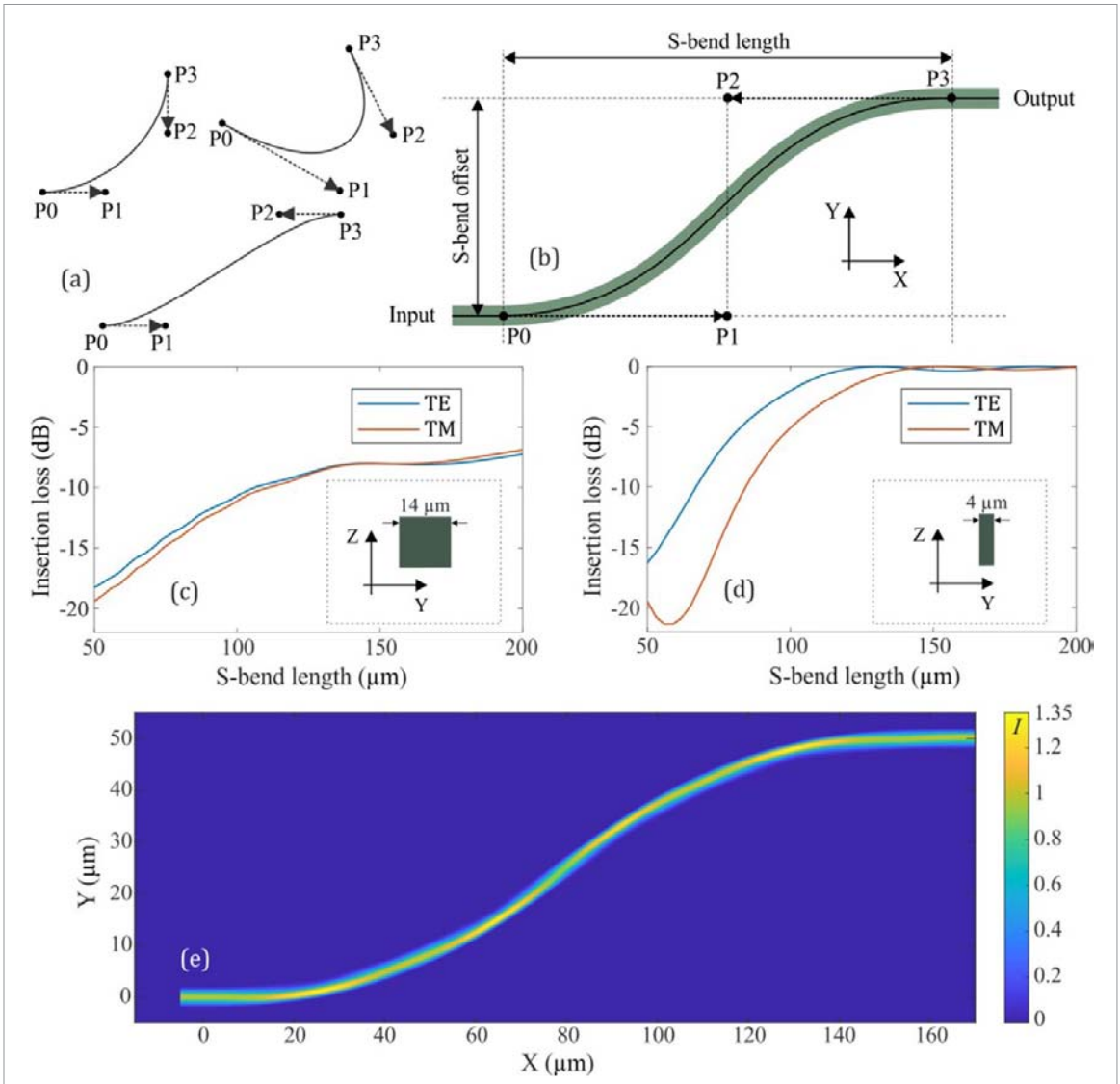

Figure 6. (a) Examples of Bezier curves defined by four control points. (b) Top view of an S-bend and definitions of its main geometrical parameters. Modeling results for S-bend insertion loss for two orthogonally polarized fundamental modes that offsets the waveguide by 50 μm using (c) 14 × 14 μm^2 and (d) 14 × 4 μm^2 cross-section waveguides. (e) Intensity distribution in a 160 μm long S-bend that uses a waveguide with 14 × 4 μm^2 cross-section. The color scale is normalized to the intensity of the incident mode.

fundamental mode excited at the output waveguide. The oscillations caused by multimode coupling are also visible in figures 6(c) and (d): the insertion loss of the fundamental mode oscillates as the length of the S-bend is changed. For a waveguide with cross-sectional dimensions of 14 × 4 μm^2, the amplitude of these oscillations is large for shorter bend lengths and decreases as the length of the S-bends increases.

3.2. Proof-of-principle demonstration

We have fabricated the different designs described in section 3.1 using a Nanoscribe Photonic Professional GT+ 3D printing workstation and we have measured the insertion loss of these samples as well as their transmission spectra, as explained in section 2.

First, we have fabricated two sets of 14 × 14 μm^2 square and 15 μm diameter waveguides with lengths varying between 200 μm and 1 mm. One set of circular waveguides is shown in figure 7(a). Recall that the cross-sectional dimensions of the waveguides were chosen to achieve best mode matching with the fundamental mode of an SMF-28® optical fiber, and that the supporting ridge dimensions were selected to have negligible influence on the optical waveguiding properties of the waveguides. An SEM image of a 400 μm long rectangular waveguide on top of the support structure with V-grooves at both sides is shown in figure 7(b). SEM images of the square and circular waveguides are shown in figures 7(c) and (d), respectively. The ridge that separates the waveguide from the support base is visible as well.

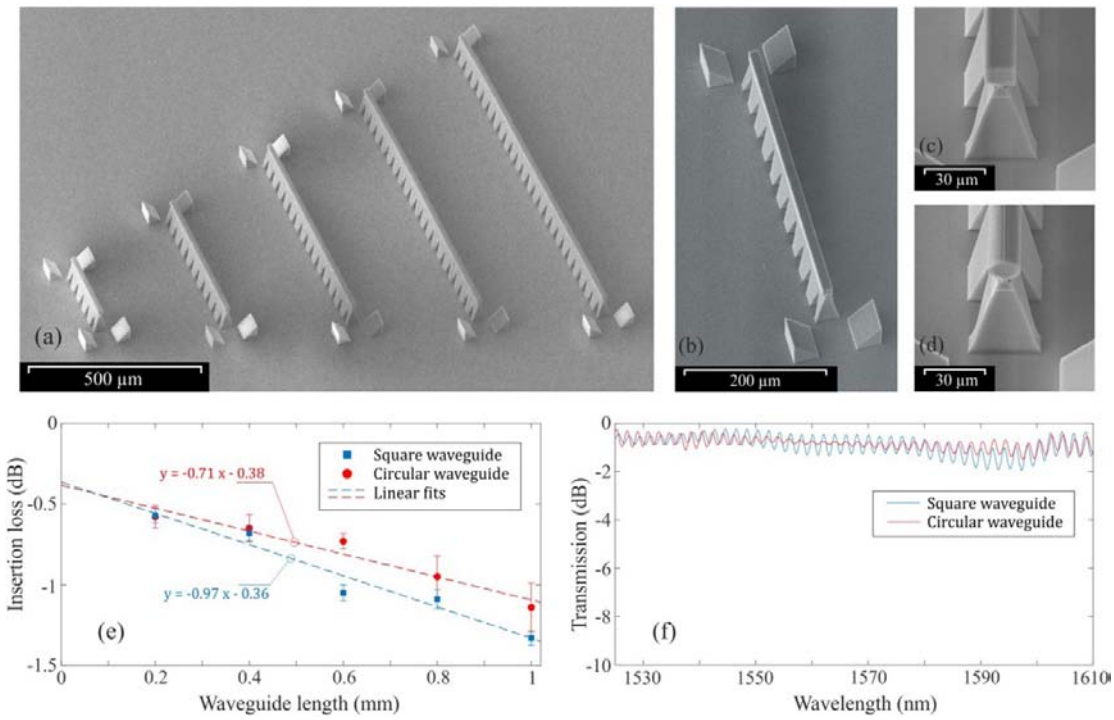

Figure 7. (a) Scanning electron microscope (SEM) image of an array of 3D-printed circular cross-section waveguides with lengths from 0.2 to 1 mm on support bases—the V-grooves for optical fiber positioning are visible as well. (b) SEM image of a 400 μm long waveguide with square cross-section, as well as front views of waveguides with (c) square and (d) circular cross-sections. (e) Average insertion loss values and the standard deviation measured with a broadband source in the range from 1525 to 1610 nm for all waveguides of different lengths. The dashed lines are linear regressions, the slopes of which correspond to the propagation loss values (see also section 4). (f) Transmission spectra of 400 μm long waveguides.

Figure 7(e) shows the average insertion loss and standard deviation measured for two samples obtained with a broadband unpolarized source in the 1510–1625 nm range. Remarkably, for all the considered waveguides with length up to 1 mm, the insertion loss stays below −1.5 dB. For both square and circular 200 μm long waveguides, we find similar mean insertion loss values around −0.6 dB. Note that in section 3.1.1 we have predicted a minimal insertion loss around −0.2 dB per fiber-waveguide interface, so the theoretically predicted loss for interfacing the waveguide with two fibers is −0.4 dB. The difference between square and circular shapes becomes noticeable as the waveguide length increases. The square waveguide returns an insertion loss slightly higher for lengths starting from 600 μm. These results indicate that a circular waveguide is more favorable in view of the lower propagation loss for longer lengths, but for lengths up to 400 μm the performance is very much comparable to that of circular waveguides.

We have also carried out spectral transmission measurements of the fabricated straight waveguides. To do so, we used an ASE source from NP Photonics operating in the spectral range from 1525 to 1610 nm, and an ANDO Optical Spectrum Analyzer. The results for 400 μm long waveguides with square and circular cross-sections are shown in figure 7(f). First, we observe oscillations in the transmission spectra for both waveguides. This is well known to occur when a multimode waveguide is placed in between two single-mode waveguides. The oscillation of the output power stems from the excitation of the closest higher order mode of the multimode waveguide and the resulting multimode interference [29, 30]. Hence, the oscillation period also depends on the length of the waveguide. Several devices including sensors and lasers exploit this effect. Possible causes of higher-order mode excitation in our components can be the surface roughness of the waveguides and the sub-optimal light launching conditions from the SMF-28® fiber to the 3D-printed waveguides. Although it is difficult to completely eliminate such oscillations given the multimode nature of the 3D-printed waveguide, their amplitude could be decreased by optimizing the fabrication parameters and the alignment. Apart from the presence of these oscillations though, we clearly see the very low wavelength dependence of the waveguides in the C- and L-band, which agrees well with our simulation results.

Second, we have fabricated rectangular and circular tapers and we also characterized the insertion loss of these components. To start with, we consider tapering down from a waveguide with a square cross-section of 14×14 μm^2 mode matched with an SMF-28® fiber to a 14×2 μm^2 cross-section waveguide such that adiabatic coupling of the fundamental mode is enabled. The simulations tell that this can be achieved with a parabolic and 55 μm long taper featuring $\alpha = 3.4$. To study this experimentally, we have fabricated a 400 μm

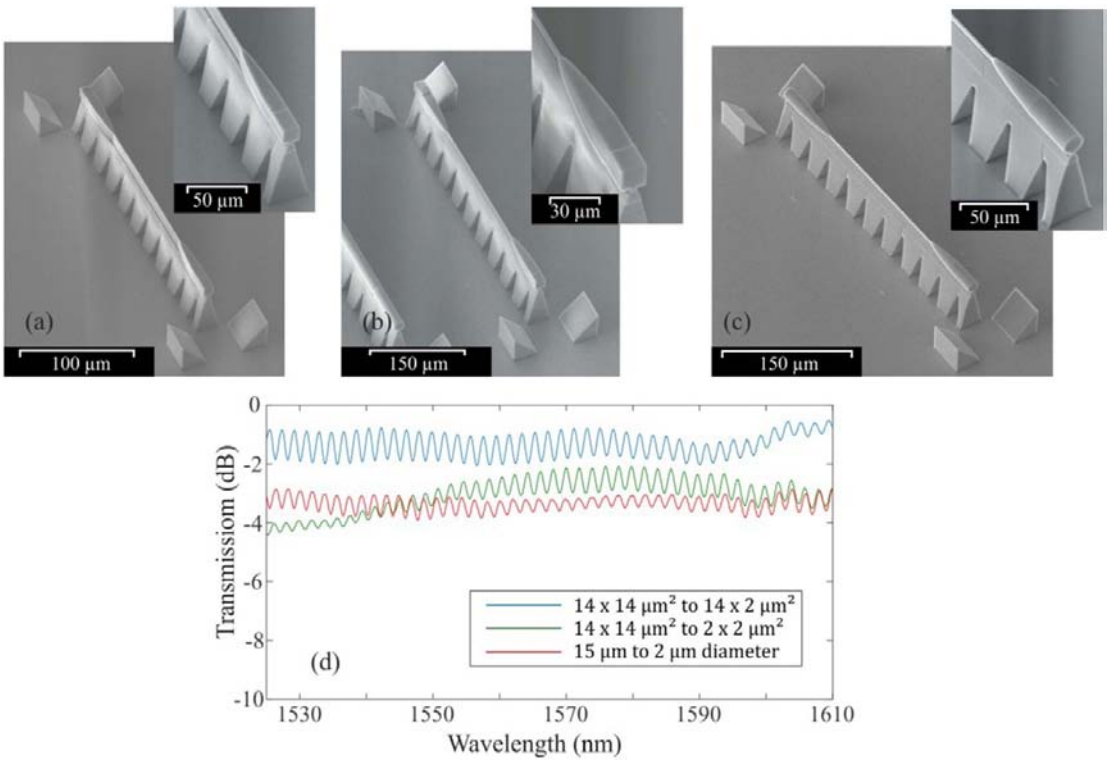

Figure 8. SEM images of 400 μm long components with tapers for adiabatic transition from (a) 14 $\times$ 14 μm^2 to 14 $\times$ 2 μm^2 cross-sections; (b) 14 $\times$ 14 μm^2 to 2 $\times$ 2 μm^2 cross-sections; and (c) 15 μm to 2 μm diameter cross-sections. (d) Transmission spectra of the waveguides with tapers.

long component, which consists of a 40 μm long straight waveguide section with a 14 $\times$ 14 μm^2 cross-section for in-coupling light from a fiber, the 55 μm long adiabatic down-taper, a 210 μm long section of the waveguide with a 14 $\times$ 2 μm^2 cross-section, followed by another up-taper and a 40 μm long straight waveguide section for out-coupling light to a fiber. An SEM image of the fabricated component is shown in figure 8(a). For the three fabricated identical structures, we measured an average insertion loss and standard deviation of -1.03 ± 0.08 dB. The average insertion loss of a straight waveguide with a 14 $\times$ 14 μm^2 cross-section and identical length was -0.68 dB. Considering that we can expect higher propagation loss for a 210 μm long waveguide with a 14 $\times$ 2 μm^2 cross-section, the excess loss of -0.35 dB is an excellent demonstration of the nearly adiabatic performance of the tapers.

We then also fabricated tapers for a transition from a 14 $\times$ 14 μm^2 cross-section waveguide to one with a 2 $\times$ 2 μm^2 cross-section. An identical parabolic shape of the tapers with $\alpha = 3.4$ was used for tapering along the two cross-sectional dimensions of the waveguide. We used the same configuration as above with input and output waveguides and a 210 μm long section of the waveguide with a 2 $\times$ 2 μm^2 cross-section. A SEM image of one of the fabricated components is shown in figure 8(b). The average insertion loss and standard deviation measured for three identical structures for fiber-to-fiber coupling through the 400 μm long components is -2.48 ± 0.24 dB. This is higher than the previous case and can be explained by the smaller size and the geometry of the taper. Note that we used a taper shape that has been optimized in view of tapering along one cross-sectional dimension of the waveguide. We project that additional optimization of the shape for tapering along the two dimensions can result in lower insertions loss.

To end our study on tapers, we have fabricated circular tapers for transitioning from a 15 μm diameter waveguide to a 2 μm diameter waveguide, as shown in figure 8(c). The optimal taper shape for such a transition uses $\alpha = 4.2$ and measures 43.2 μm in length. The entire component was 400 μm long, and consisted of a 40 μm long straight input waveguide with a 15 μm diameter, a 43.2 μm long adiabatic down-taper, a 233.6 μm long waveguide section with a 2 μm diameter, followed by an identical up-taper and a 40 μm long straight waveguide section for out-coupling to an SMF-28® fiber. The average insertion loss and standard deviation for three identical structures is -2.96 ± 0.17 dB. For the sake of comparison, 15 μm diameter straight waveguides with an identical length returned an average insertion loss of -0.65 dB.

For these three types of tapered components, we have also carried out spectral measurements using an unpolarized ASE source. The measured spectra are shown in figure 8(d). Similar to those obtained with the straight waveguides, we observe oscillations that we relate to higher-order mode excitation and multimode

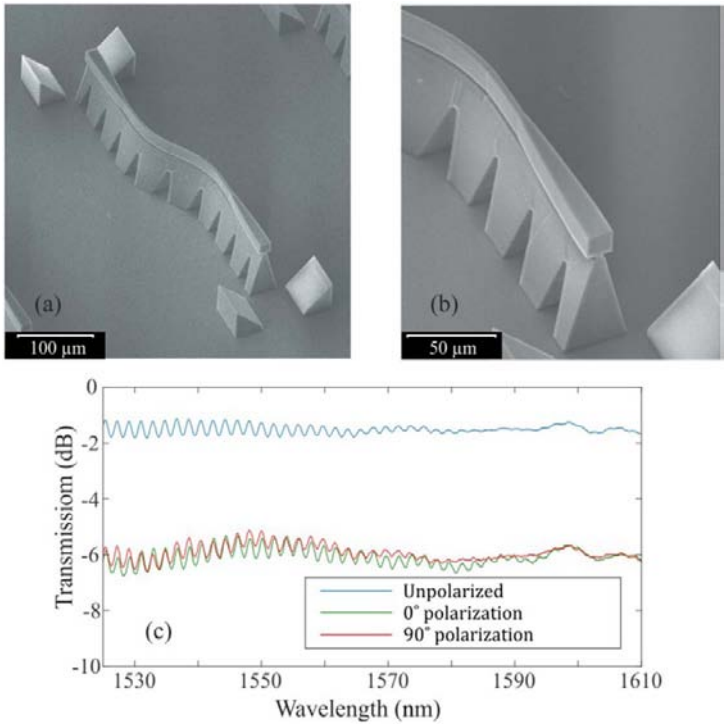

Figure 9. SEM images of S-bends for a waveguide offset of 50 μm over a length of 160 μm, using a waveguide with a 14 $\times$ 4 μm^2 cross-section. (c) Transmission spectra for one of the S-bends.

interference. Here also, we observe a relatively weak dependence on the wavelength, which again agrees well with our simulations. Only for square-shaped waveguides with the largest transition in terms of cross-sectional area, i.e. from a 14 $\times$ 14 μm^2 to 2 $\times$ 2 μm^2, we observe a higher transmission in the 1575 nm wavelength range, and lower transmission values at shorter and longer wavelengths.

Third and finally, we have fabricated S-shaped waveguide bends according to the design described in section 3.1.3 with the intention to offset a waveguide axis by 50 μm. The waveguide has a 14 $\times$ 4 μm^2 cross-section and we designed a dedicated taper for adiabatic transition to a 14 $\times$ 4 μm^2 cross-section using the results given in figure 4(c). Such a taper uses $\alpha = 2.5$ and measures 73 μm in length. The total length of the component is 396 μm and consists of a 20 μm long straight waveguide section with a 14 $\times$ 14 μm^2 cross-section for in-coupling of light from the fiber, the 73 μm long adiabatic taper, a 20 μm long straight waveguide section with a 14 $\times$ 4 μm^2 cross-section, a 170 μm long section of an S-bend waveguide with a 14 $\times$ 4 μm^2 cross-section, followed by symmetric sections for out-coupling light to a fiber. Figure 9 shows SEM images of one of the fabricated components. The average insertion loss and standard deviation for 3 identical samples is -1.69 ± 0.02 dB. We can compare this value to that of -1.03 dB of the component in figure 8(a), which relied on two tapers with a straight waveguide section. Despite the presence of a bent section, the loss level is only -0.66 dB higher, which confirms that we used an adequate strategy for designing low loss adiabatic S-bends. For the S-shaped waveguide bends, we also carried out spectral transmission measurements, which are depicted in figure 9(c). When using an unpolarized ASE source, we obtain transmission spectra with a low wavelength dependence, comparable to what we observed for the straight waveguides. For longer wavelengths, we also see that the oscillations resulting from multimode interference are weakened, which might depend on the shape of the waveguide curvature. We plan to study the extent of this effect further in our future research. For this component, we also measured transmission spectra for two orthogonal polarizations by using a polarizer and a half-wave plate. The decrease of the transmission level for the polarized light is caused by the addition of polarizing components to the setup, while the transmission is still normalized to the unpolarized light. We see no significant polarization dependence, and for orthogonal polarizations, we find a wavelength dependence that is almost identical to that with unpolarized light.

4. Discussion

We have developed an approach for the 3D-printing of optical waveguide structures and for measuring their insertion losses, as illustrated in figure 1. This is an enabling step for reliable experimental verification of numerical designs and optimizations of optical waveguides. We have based our approach on reports in open

literature in which authors raised the component under study above the level of the planar substrate using mechanical supports [18, 19]. We have added V-grooves for alignment and positioning, periodic openings allowing to counteract delamination, as well as supporting ridges, and we have implemented a two-step writing process for the mechanical (support) and optical components with different printing parameters, which resulted in fast and robust component fabrication with lengths up to 1 mm. This is exemplified in figure 7(a) with an array of five waveguides with circular cross-section, which took 2 h in terms of fabrication time with subsequent development of the sample in propylene glycol methyl ether acetate for 5 min.

At the same time, the availability of pre-printed V-grooves speeds up the required high-accuracy alignment and centering of the single-mode optical fiber cores with the waveguides and enables repeatable insertion loss measurements. Our strategy, however, may still raise concerns—especially in the case of straight (and tapered) waveguides—since the two fibers for in- and out-coupling are aligned along a single axis. The risk is that, since the fabricated components are fairly short, light emitted from one fiber may couple directly into the other without being guided by the 3D-printed component. This problem may be exacerbated if the tested components are smaller in cross-section compared to the core of the fibers and when manual alignment is used. Note however, that our 3D-printed waveguides had cross-sectional dimensions that mostly exceeded these of the fiber core and that our alignment strategy with V-grooves allowed for sub-micrometer accuracy. To confirm that no light is being coupled from fiber to fiber without passing through the components, we have fabricated a waveguide with a distorted central region that scattered all the light out of the component. We measured almost no light coupled from one fiber to another. The results for the S-bends with offset axes are another evidence that our results for on axis measurements are very reliable.

Figure 7(e) shows the insertion loss measurement results for straight waveguides with different lengths. Such measurements can be used to estimate propagation and coupling losses in waveguides. From these results and by applying a linear regression as shown in figure 7(e) with dashed lines, we find a propagation loss of -0.97 dB mm^{-1} and a waveguide-to-fiber coupling loss of -0.18 dB for waveguides with a square cross-section. For waveguides with a circular cross-section, the estimated propagation loss is -0.71 dB mm^{-1} and the waveguide-to-fiber coupling loss is -0.19 dB. Note that these estimates for the waveguide-to-fiber coupling loss are in perfect agreement with the simulation results shown in figure 2, where we estimated a minimal loss value of -0.19 dB. On the other hand, the accuracy of the estimates of the propagation loss might be compromised by two elements. First, with our 3D-printing approach and when the length of the printed structures exceeds the field of view of the microscope objective used for the printing (150 μm in our case), the object is split into separate portions with each portion being printed sequentially. These different portions are stitched to each other with a certain stitching accuracy that is limited by the translation stage positioning and alignment errors. Stitching can be observed in the SEM images of the waveguide components shown in figures 7–9 and can cause additional loss in the waveguide. Hence the uncertainty on the propagation loss estimate in influence by excess loss caused by stitching errors and due to the number of stitches used for printing the waveguides. Second, the data shown in figure 7(e) uses measurements of only two sets of waveguides. A more accurate estimation would require more measurements to reach better statistical significance, but this is out of the scope of this paper.

For the low-loss S-bends shown in figure 9, we used Bezier curves for defining the shape of the curvature. To allow for a comparison with other fabrication techniques reported in literature, we have also estimated the radius of curvature of the bend. The 160 μm long S-bend that shifts the waveguide axis by 50 μm can be best approximated by circular arcs with a radius of curvature equal to 140 μm. This highlights one advantage of the 3D direct laser writing in polymers over direct femtosecond laser writing (FLW) in glass. With the latter, waveguides are inscribed with laser-induced refractive index modifications in the bulk of glass material. The resulting refractive index contrast between core and cladding are relatively small, leading to bending radii of the order of tens of millimeters [31]. With our approach instead, we do have a high index contrast as we exploit a polymer/air interface, which allows working with substantially smaller bending radii. More recently though, a new technique for inducing higher refractive index changes with FLW led to record-low bending radii in the sub-millimeter range [32]. However, even the best waveguide bend still had a radius of curvature of 363 μm and featured a much more pronounced wavelength dependence. From our side, we can still expect to further decrease the radius of curvature by optimizing the designs and the writing conditions. Literature has indeed already projected that optimizing Bezier curve shapes would allow achieving sharper bends and lower losses [27, 33].

Finally, we emphasize that while most of the waveguide components demonstrated in the paper are few-moded or highly multimodal, all our numerical analyses were based on calculations that only consider the fundamental modes. This also means that all the insertion loss results presented in the paper were calculated for coupling of the fundamental mode of the input waveguide to the fundamental mode of the output waveguide. Note that for the experimental characterization of the insertion loss of the samples, we have always used SMFs, which automatically filtered higher orders in the measured data. Although working

with higher order modes can be beneficial in view of considering multimode waveguide-based applications [34] in optical communication and interconnects, and even in sensing, accurate control over propagation in the fundamental mode of the waveguide must be prioritized.

5. Summary and conclusions

Our overarching objective was to define a strategy based on which design rules for several building blocks for 3D-printed integrated photonic waveguide devices, fabricated with 2PP-based direct laser writing, can be developed. To pursue that goal, we have proposed and developed a dedicated methodology for optimizing a suite of selected photonic waveguide components. The enabling step consists in raising the components above the level of the substrate by means of 3D-printed mechanical support structures and pre-printing V-grooves for accurate fiber alignment. This allows for fast and repeatable insertion loss measurements of a series of components and for reliable comparison of the measurement results with the simulations. In addition, all the devices demonstrated in our paper have been fabricated with a galvo-mirror enabled high-speed scanning regime, which also allows for fast and repeatable prototyping and subsequent testing of such devices. As a result, we were able to demonstrate a series of low-loss waveguide components that all feature an insertion loss well below −3 dB in the wavelength range from 1500 nm to 1600 nm, with very low polarization dependence.

First, our modeling results revealed that waveguides with a square cross-section of $14 \times 14\ \mu m^2$ and with a circular cross-section diameter of 15 μm provide for optimal free-space coupling efficiency to standard telecom SMF-28® fibers. We have fabricated square and circular cross-section waveguides with lengths varying from 0.2 mm to 1 mm. We achieved a minimal total insertion loss less than −0.6 dB with 0.2 mm long waveguides and two fiber-to-waveguide coupling facets, which exceeds the theoretically predicted minimal coupling loss for two fiber-waveguide interfaces by only −0.4 dB. For waveguides with square and circular cross-sections and lengths up to 1 mm, the average insertion loss did not exceed −1.5 dB, whilst for square cross-sections the loss was slightly higher (for 0.6 mm, 0.8 mm and 1 mm long waveguides).

Second, we have studied adiabatic tapers for waveguide size conversion, and we have identified optimal parabolic shapes for both rectangular and circular cross-section waveguide tapers which allow for lossless propagation of the waveguide's fundamental mode. We found that for parabolic tapers, when tapering down to smaller waveguide sizes starting from the same cross-section, shorter taper lengths can be more efficient. For example, going from a $14 \times 14\ \mu m^2$ square cross-section waveguide to a $14 \times 6\ \mu m^2$ waveguide requires a 118 μm taper for an adiabatic transition, whilst the required length decreases to 55 μm when tapering down to a $14 \times 2\ \mu m^2$ waveguide. To the best of our knowledge, such a behavior of tapers is reported for the first time and may be specific for the materials with refractive indices close to that of IP-Dip®, which is the material of choice considered in this study. We have fabricated such tapers and we succeeded in experimentally demonstrating that parabolic tapers do add minimal insertion loss.

Third and finally, we have numerically studied Bezier curve-based S-bends and we have identified an approach for low loss and short length waveguide axis offsetting, whilst keeping the optical energy in the fundamental mode. We were able to obtain nearly losses S-bend configurations that outperform regular S-bends by first tapering the fiber-coupling waveguide to a smaller cross-section by means of adiabatic tapers. As a proof-of-principle, we have fabricated S-bends using a $14 \times 4\ \mu m^2$ cross-section waveguide that offsets the waveguide axis by 50 μm and measures 160 μm in length. We measured a record low insertion loss of around −1.7 dB for a 400 μm long structure that included two tapers.

We anticipate that our work will prompt the researchers in the community to use optimized, low loss and efficient 3D-printed waveguide components in combination with adiabatic mode converters and bends for low-loss delivery of light when interfacing target components with optical fibers. The design rules and procedures presented in the paper provide ready-to-use recipes for fabricating and optimizing low-loss waveguide components by combining 3D-printed building blocks. The results above also allow concluding that 2PP-based fabrication of low loss waveguide components and devices holds great potential for applications where losses are a limiting factor in optical communications, sensing and even quantum optics.

Data availability statement

All data that support the findings of this study are included within the article (and any supplementary files).

Acknowledgments

Tigran Baghdasaryan is a postdoctoral Fellow of the Research Foundation—Flanders (FWO 12P1720N). The authors also wish to acknowledge partial financial support by FWO by ways of I013918N and G030217N

projects, and EOS Project G0F6218N (EOS ID 30467715). Interreg (NWE758, Fotonica pilootlijnen), Industrial Research Fund (IOF), OZR of Vrije Universiteit Brussel, Methusalem Foundation, the FWO Hercules Foundation–Flanders, COST action CA19111 are acknowledged as well.

ORCID iDs

Tigran Baghdasaryan https://orcid.org/0000-0002-6920-7363
Koen Vanmol https://orcid.org/0000-0001-9365-6866
Hugo Thienpont https://orcid.org/0000-0003-0483-0960
Francis Berghmans https://orcid.org/0000-0003-0822-233X
Thomas Geernaert https://orcid.org/0000-0002-8195-8071
Jürgen Van Erps https://orcid.org/0000-0001-7186-5907

References

[1] Maruo S, Nakamura O and Kawata S 1997 Three-dimensional microfabrication with two-photon-absorbed photopolymerization *Opt. Lett.* **22** 132
[2] LaFratta C N, Fourkas J T, Baldacchini T and Farrer R A 2007 Multiphoton fabrication *Angew. Chem., Int. Ed.* **46** 6238–58
[3] Gissibl T, Thiele S, Herkommer A and Giessen H 2016 Two-photon direct laser writing of ultracompact multi-lens objectives *Nat. Photon.* **10** 554–60
[4] Deubel M, Von Freymann G, Wegener M, Pereira S, Busch K and Soukoulis C M 2004 Direct laser writing of three-dimensional photonic-crystal templates for telecommunications *Nat. Mater.* **3** 444–7
[5] Lindenmann N, Dottermusch S, Goedecke M L, Hoose T, Billah M R, Onanuga T P, Hofmann A, Freude W and Koos C 2015 Connecting silicon photonic circuits to multicore fibers by photonic wire bonding *J. Lightwave Technol.* **33** 755–60
[6] Billah M R *et al* 2018 Hybrid integration of silicon photonics circuits and InP lasers by photonic wire bonding *Optica* **5** 876
[7] Gao H, Chen G F R, Xing P, Choi J W, Low H Y and Tan D T H 2020 High-resolution 3D printed photonic waveguide devices *Adv. Opt. Mater.* **8** 2000613
[8] Wei H and Krishnaswamy S 2017 Polymer micro-ring resonator integrated with a fiber ring laser for ultrasound detection *Opt. Lett.* **42** 2655
[9] Kelemen L, Lepera E, Horváth B, Ormos P, Osellame R and Martínez Vázquez R 2019 Direct writing of optical microresonators in a lab-on-a-chip for label-free biosensing *Lab Chip* **19** 1985–90
[10] Gehring H, Blaicher M, Hartmann W, Varytis P, Busch K, Wegener M and Pernice W H P 2019 Low-loss fiber-to-chip couplers with ultrawide optical bandwidth *APL Photonics* **4** 010801
[11] Vanmol K, Tuccio S, Panapakkam V, Thienpont H, Watté J and Van Erps J 2019 Two-photon direct laser writing of beam expansion tapers on single-mode optical fibers *Opt. Laser Technol.* **112** 292–8
[12] Vanmol K, Saurav K, Panapakkam V, Thienpont H, Vermeulen N, Watte J and Van Erps J 2020 Mode-field matching down-tapers on single-mode optical fibers for edge coupling towards generic photonic integrated circuit platforms *J. Lightwave Technol.* **38** 4834–42
[13] Vanmol K, Baghdasaryan T, Vermeulen N, Saurav K, Watté J, Thienpont H and Van Erps J 2020 3D direct laser writing of microstructured optical fiber tapers on single-mode fibers for mode-field conversion *Opt. Express* **28** 36147
[14] Kumar A, Nambiar S, Kallega R, Ranganath P, Ea P and Selvaraja S K 2021 High-efficiency vertical fibre-to-polymer waveguide coupling scheme for scalable polymer photonic circuits *Opt. Express* **29** 9699
[15] Wei H and Krishnaswamy S 2019 Direct laser writing of a phase-shifted Bragg grating waveguide for ultrasound detection *Opt. Lett.* **44** 3817
[16] Wei H, Amrithanath A K and Krishnaswamy S 2018 Three-dimensional printed polymer waveguides for whispering gallery mode sensors *IEEE Photonics Technol. Lett.* **30** 451–4
[17] Zhang S *et al* 2019 High- Q polymer microcavities integrated on a multicore fiber facet for vapor sensing *Adv. Opt. Mater.* **7** 1900602
[18] Wei H and Krishnaswamy S 2016 Direct laser writing polymer micro-resonators for refractive index sensors *IEEE Photonics Technol. Lett.* **28** 2819–22
[19] Goraus M, Pudis D, Urbancova P, Martincek I and Gaso P 2018 Surface-relief Bragg grating waveguides based on IP-Dip polymer for photonic applications *Appl. Surf. Sci.* **461** 113–6
[20] Lumerical Inc. *High-Performance Photonic Simulation Software — Lumerical* (available at: www.lumerical.com/) (Accessed 18 August 2021)
[21] Nanoscribe GmbH *Think big. Print nano. Your partner for high-precision additive manufacturing* (available at: www.nanoscribe.com/en/) (Accessed 18 August 2021)
[22] Dottermusch S, Busko D, Langenhorst M, Paetzold U W and Richards B S 2019 Exposure-dependent refractive index of nanoscribe IP-Dip photoresist layers *Opt. Lett.* **44** 29
[23] Karioja P and Howe D 1996 Diode-laser-to-waveguide butt coupling *Appl. Opt.* **35** 404
[24] Milton A and Burns W 1977 Mode coupling in optical waveguide horns *IEEE J. Quantum Electron.* **13** 828–35
[25] Fu Y, Ye T, Tang W and Chu T 2014 Efficient adiabatic silicon-on-insulator waveguide taper *Photonics Res.* **2** A41
[26] Hammer M and Ivanova O V 2009 Effective index approximations of photonic crystal slabs: a 2-to-1-D assessment *Opt. Quantum Electron.* **41** 267–83
[27] Bahadori M, Nikdast M, Cheng Q and Bergman K 2019 Universal design of waveguide bends in silicon-on-insulator photonics platform *J. Lightwave Technol.* **37** 3044–54
[28] Farin G 1983 Algorithms for rational Bézier curves *Comput. Des.* **15** 73–7
[29] Wu Q, Semenova Y, Wang P and Farrell G 2011 High sensitivity SMS fiber structure based refractometer—analysis and experiment *Opt. Express* **19** 7937

[30] Zhu X, Schülzgen A, Li H, Li L, Wang Q, Suzuki S, Temyanko V L, Moloney J V and Peyghambarian N 2008 Single-transverse-mode output from a fiber laser based on multimode interference *Opt. Lett.* **33** 908
[31] Osellame R, Cerullo G and Ramponi R 2012 *Femtosecond Laser Micromachining* vol 123, ed R Osellame, G Cerullo and R Ramponi (Berlin: Springer) (https://doi.org/10.1007/978-3-642-23366-1)
[32] Lapointe J, Bérubé J-P, Ledemi Y, Dupont A, Fortin V, Messaddeq Y and Vallée R 2020 Nonlinear increase, invisibility, and sign inversion of a localized fs-laser-induced refractive index change in crystals and glasses *Light Sci. Appl.* **9** 64
[33] Yi D, Zhang Y and Tsang H K 2021 Optimal Bezier curve transition for low-loss ultra-compact S-bends *Opt. Lett.* **46** 876
[34] Li C, Liu D and Dai D 2018 Multimode silicon photonics *Nanophotonics* **8** 227–47